# Stress Distribution of EH40 with Defects Considering Solid-State Phase Transformation

## The effects of weld defects and SSPT on residual stress of marine steel EH40 in high-power laser welding were analyzed

BY L. WANG, Y. RONG, Y. HUANG, J. XU, J. HU, AND G. ZHANG


## Abstract

Residual stress of laser-welded marine steel EH40 was experimentally and numerically analyzed considering weld defects (collapse, hump, and unfitness) and solid-state phase transformation (SSPT). A double-cylindrical source model was used to simulate the temperature distribution. The mean prediction errors of the model without and with weld defects along the plate thickness were 9.2 and 3.5%. Based on the thermodynamics of SSPT, microstructure fractions were computed and verified by weld hardness test results. Under the effect of SSPT, residual stress changed from compressive stress to tensile stress with the increase of the distance from the weld center. Weld defects have an influence on the value of residual stress, and this effect was greater when SSPT was considered. The affected zone extended from the vicinity of weld defects to the whole weld. The variations of longitudinal residual stress (LRS) and transverse residual stress (TRS) caused by weld defects and SSPT both exceeded 150 MPa. LRS was mainly affected by the loss and increase of metal, while TRS was affected by the stress concentration caused by shape geometry changes. Thus, the influence of weld defects on TRS was greater than that on LRS. The proposed finite element model considering weld defects and SSPT can be used to accurately predict residual stress in laser welding of marine steel EH40 and provide a theoretical basis to reduce welding stress.



## Keywords

- Laser Welding
- Weld Defects
- Solid-State Phase Transformation
- Marine Steel
- Residual Stress


## Introduction

Marine equipment is becoming large scale, diversified, and high performing, and, thus, high-strength steel with large thickness is more and more widely used. High-power laser welding (≥ 10 kW), owing to its advantage in high-energy density, small heat-affected zones (HAZs), and high-efficiency processing, becomes an effective way to realize a thick-plate (≥ 10 mm [0.39 in.]) single-pass joining. A complete joint penetration 304 stainless steel joint with a thickness of 12 mm (0.47 in.) could be welded by a 10-kW laser during bead-on-plate welding (Ref. 1). Meng et al. (Ref. 2) achieved high-quality complete joint penetration welded joints with a thickness of 15 mm (0.59 in.) by using a pulse fiber laser. Under reduced ambient pressure, Jiang et al. (Ref. 3) realized the single-pass laser welding of 20-mm- (0.79-in.-) thick high-strength steel without weld defects. Kawahito et al. (Ref. 4) obtained a single-pass weld bead depth of 70 mm (2.76 in.) by a 100-kW fiber laser. However, during high-power laser welding, the heat distribution exhibits a highly inhomogeneous state, leading to a high gradient of residual stress and affecting joint performance (Ref. 5).

The inhomogeneous residual stress in the thickness direction cannot be ignored for thick-plate welding. The study of Yang et al. (Ref. 5) showed that the distributions of transverse residual stress (TRS) and longitudinal residual stress (LRS) are inhomogeneous, and the peak of residual stress was located near the plate surface. Combining the finite element analysis and experimental measurements, Banik et al. (Ref. 6) investigated through-thickness residual stress. The TRS and LRS fluctuated obviously, and the fluctuation exceeded 150

https://doi.org/10.29391/2023.102.024

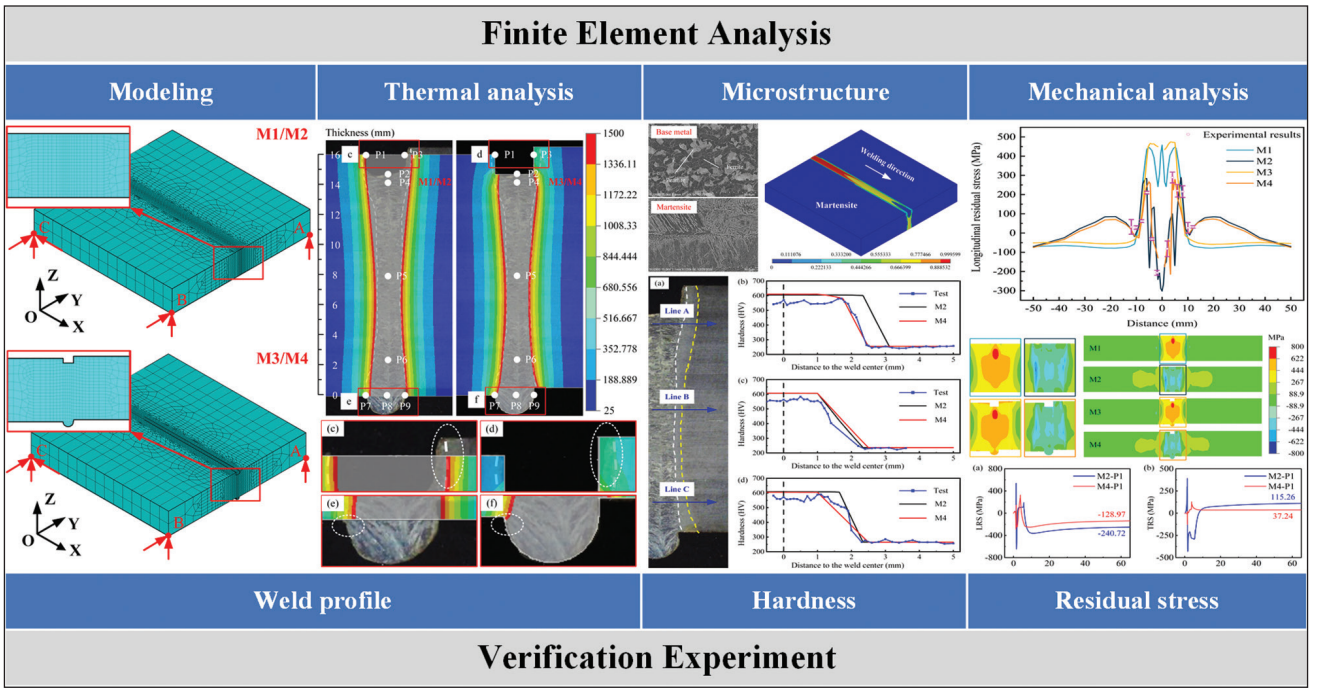


*Fig. 1 — Simulation and experiment implementation framework of marine steel EH40 welded joint.*

MPa. Ibrahim et al. (Ref. 7) found that the thicker the welded plate, the greater the fluctuation in the through-thickness residual stress. Xu et al. (Ref. 8) compared the residual stress distribution at different thicknesses of welded joints and found that the longitudinal stresses had similar distribution features, while the transverse residual stresses at the middle part of the welded joint had an opposite distribution feature to that at the top and bottom surfaces of the welded joint. This indicated the self-constraint caused by plate thickness had a larger effect on the distribution of TRS.

Hump formation is a common weld defect in the single-pass forming of large-thickness plates (Refs. 9, 10), and collapse usually occurs at the same time. In addition, unfitness is also common in upset welding (Ref. 11). The residual stress distribution and welding deformation are both impacted by these geometrical defects. Liang et al. (Ref. 12) studied the formation of the hump and its effect on residual stress using a coupled computational fluid dynamic-finite element method (CFD-FEM) model and found that the hump caused stress concentration and increased the localized von Mises stress. Xia and Jin (Ref. 13) analyzed the residual stress of austenitic stainless steel butt joints with dissimilar thicknesses in different butt joint forms and concluded that the distribution and amplitude of residual stress were influenced by the weld geometry.

With a deeper understanding of the residual stress formation mechanism, the traditional thermo-elastic-plastic finite element method (TEP-FEM) cannot simulate the microstructure field in the joint. In the actual welding process, solid-state phase transformation (SSPT) always occurs from austenite to other phase mixtures. These transformations are accompanied by an increase in volume at the microscopic level, which affects the final residual stress distribution. The research of Wang et al. (Ref. 18) showed that the accumulation of tensile residual stress was offset because of the volumetric expansion during martensite transformation. This results in a decrease in welding residual tensile stress, the formation of a stable compressive stress segment in the fusion zone (FZ), and a reduction in welding deformation. Welding residual stress and deformation are significantly impacted by SSPT.

Many research achievements have been made on the effect of plate thickness, weld defects, and SSPT on residual stress distribution during laser welding. However, in high-power laser welding, the high-power density energy input causes the residual stress gradient to grow, and the thick plate further aggravates the residual stress's inhomogeneous distribution. Meanwhile, the distribution of residual stress under the combined action of various welding defects (collapse, hump, and unfitness) and SSPT has not been methodically analyzed. In this combined experiment and simulation study, the influence of weld defects and SSPT on residual stress was investigated, working with 16-mm- (0.63-in.-) thick marine steel EH40. Four 3D transient coupled thermostructural models were developed to study the stress distribution considering weld defects (collapse, hump, and unfitness) and SSPT. The simulation and experiment implementation framework are shown in Fig. 1. First, two models with and without weld defects were built to compute the thermal-metallurgical-mechanical field. The weld profile was used to test the validity of the thermal

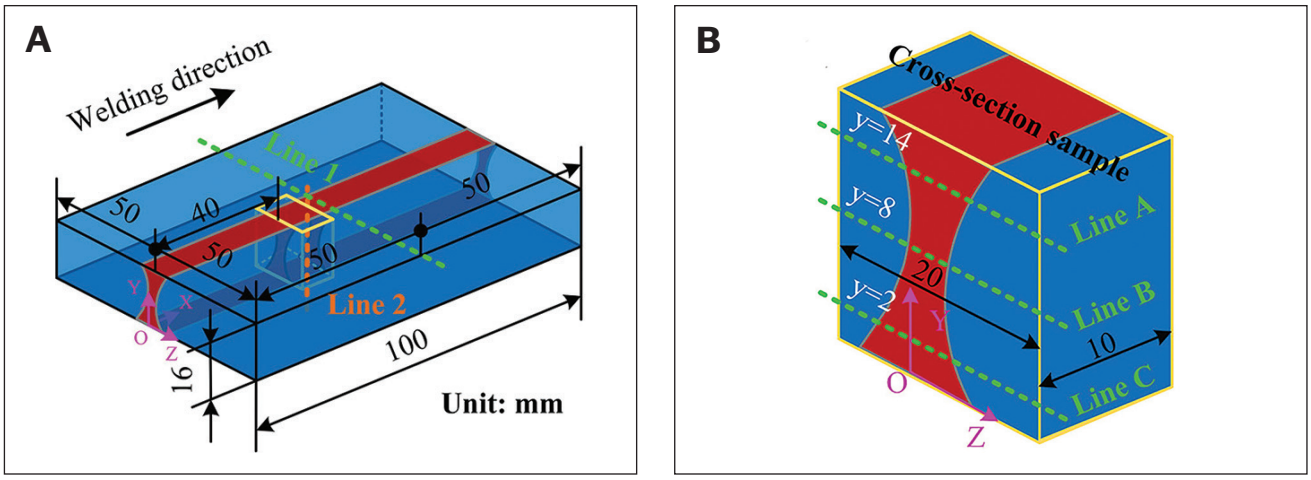


*Fig. 2 — A — The size of the EH40 butt joint, the test position (Line 1) of residual stress; B — Line A, Line B, and Line C of hardness.*

**Table 1 — Chemical Composition of EH40 Steel (wt-%)**

| C | Si | Mn | P | S | Al | Cr | Nb | V | Ti | Ni | Cu | Fe |
|---|---|---|---|---|---|---|---|---|---|---|---|---|
| 0.12 | 0.31 | 1.31 | 0.018 | 0.0041 | 0.021 | 0.04 | 0.01 | 0.003 | 0.012 | 0.02 | 0.02 | Bal. |

field. Then, the distribution of microstructure was obtained by experiment and simulation. Due to the deep correlation between hardness and microstructure, the effectiveness of the SSPT model was verified by comparing experimental and simulated hardness values at different thicknesses. Finally, the residual stress distribution of welded joints and the evolution process of nodes affected by weld defects and SSPT were investigated and analyzed.

# Experiment

## Experiment Details

A welding experiment was designed with a butt joint. The base metal (BM) was marine steel EH40 with a size of 50 × 100 × 16 mm (1.97 × 3.94 × 0.63 in.), as shown in Fig. 2A, and its chemical components are given in Table 1. The welding system mainly consisted of a fiber laser IPG YLS-30000, KUKA robot, laser header, jig, and platform. The laser power was 25 kW, the welding speed was 2.1 m (6.89 ft)/min, the defocus length was 0 mm, and the shielding gas was argon with a flow of 2.1 $m^3$/h. Before welding, the sample surface was milled to remove the oxide layer and cleaned with acetone to reduce the impact of dust and oil contamination.

## Measurement Methods

After welding, an x-ray stress analyzer was used to quantify residual stress along Line 1, as shown in Fig. 2A. The section sample was extracted by wire electrical discharge machining and eroded using a solution of HNO3: Alcohol = 4:96 to obtain the weld geometry. The microstructure of the weld was observed by an optical microscope and scanning electron microscopy (SEM). The distributions of hardness along Line A, Line B, and Line C were measured with a Vickers microhardness tester, as shown in Fig. 2B, and a load of 300 g (10.58 oz) and a dwell period of 15 s were used.

## Weld Geometry and Microstructure

The weld geometry and microstructure of the EH40 butt joint in single-pass complete joint penetration laser welding are shown in Fig. 3. Obvious weld defects were found, including collapse, hump formation, and unfitness, and their sizes were marked. The collapse's shape was roughly a rectangle with dimensions of 1.6 × 1.3 mm (0.06 × 0.05 in.), while the hump's shape resembled a semicircle with a radius of 1.25 mm (0.05 in.). And the unfitness value was 0.5 mm (0.002 in.). Furthermore, the width of both the FZ and HAZ was small compared to the plate thickness. The BM had a ferrite and pearlite microstructure, while the FZ had a martensite microstructure. In the HAZ, with the distance from the fusion line increasing, martensite decreased while ferrite increased, as shown in Figs. 3D and E.

# Numerical Analysis Process

It can be found from Fig. 3 that weld defects and SSPT both occurred in the laser-welded EH40 butt joint. The weld defects changed the weld geometry, while SSPT affected the microstructure distribution in the weld. Four models considering weld defects (collapse, hump, and unfitness) or SSPT

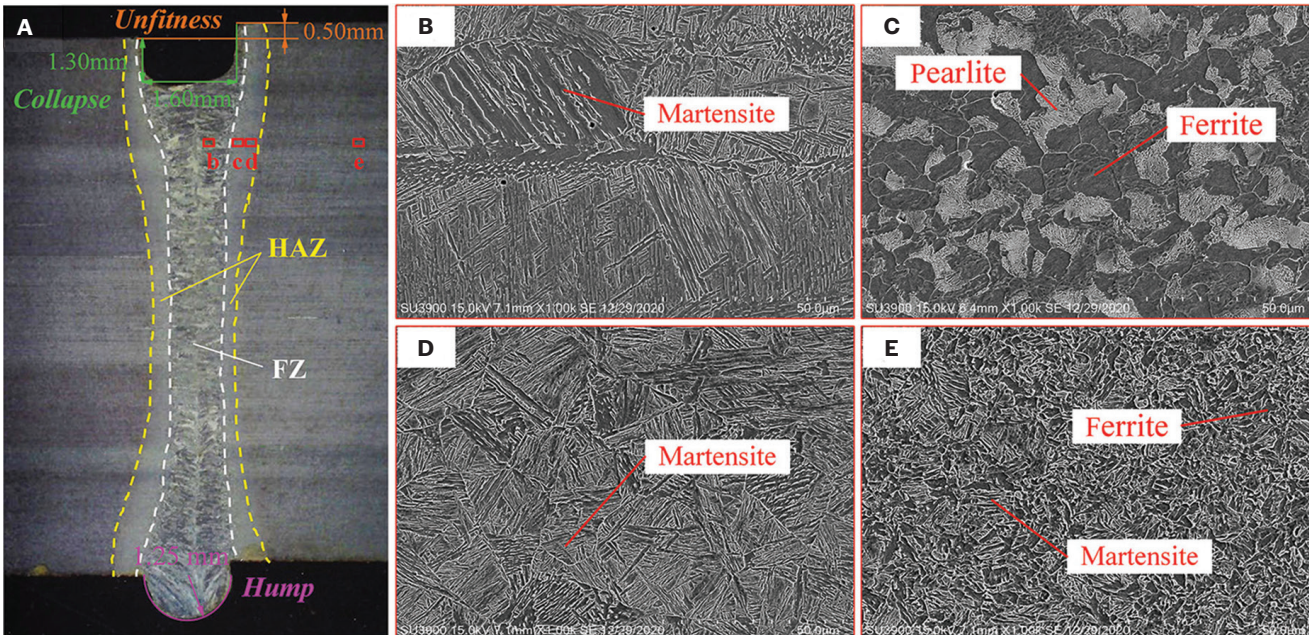


*Fig. 3 — The weld geometry and microstructure of the EH40 butt joint: A — Weld geometry (collapse, hump, and unfitness); B — the microstructure of b zone in FZ; C — c zone in BM; D and E — d and e zones in HAZ.*

**Table 2 — Four Finite Models of EH40 Steel**

| | Weld Defects | SSPT |
|---|---|---|
| M1 | × | × |
| M2 | × | √ |
| M3 | √ | × |
| M4 | √ | √ |

were established to understand their effects on the residual stress, as shown in Table 2. The distributions of temperature, microstructure, and residual stress were simulated based on the thermal-metallurgical-mechanical sequential coupling method. The geometries of the weld defects were considered in the finite element models of M3 and M4, as shown in Fig. 4B. The shapes of collapse and humps were approximated into rectangles and semicircles, and the left and right sides of the model had the same size as the unfitness. SSPT has little influence on the temperature field (Ref. 15) and thus was not considered in thermal analysis. Considering a high nonlinear characteristic of the thermal-metallurgical-mechanical behavior in laser welding, the no-uniform mesh method was adopted to improve computation efficiency and accuracy. Mesh near the FZ was refined, while mesh far from the FZ was sparse. For the finite element models without weld defects (M1 and M2), there were 53,610 elements, and most of the element sizes in the FZ were 0.667 × 0.8 × 0.5 mm (0.026 × 0.031 × 0.02 in.), whereas for the finite element models considering weld defects (M3 and M4), there were 55,120 elements, and most of the element sizes in the FZ were 0.667 × 0.8 × 0.5 mm. SOLID 70 and SOLID 185 were used in thermal analysis and mechanical analysis, respectively. In mechanical analysis, three points (A, B, and C) were constrained to prevent rigid body motion of the sample, as shown in Fig. 4.

## Thermal Analysis

A double cylindrical model was used to simulate the heating behavior (Ref. 16). This heat source model was based on the actual energy distribution of complete joint penetration welding. The peak of heat flux decays exponentially with the increased distances to the upper or bottom surfaces, thus it has great advantages in the simulation of welds with sandglass geometry. Meanwhile, most of its parameters are related to the actual welding process and can be determined by experiments. Only two coefficients need to be adjusted to improve the simulation accuracy. The mathematical expression of the double cylindrical model is shown in Equations 1–3.

$$q_0(x,y,z) = q_1(x,y,z) + q_2(x,y,z) \tag{1}$$

$$q_1(x,y,z) = \frac{9\lambda Q_{L1}}{\pi f_1^2 h_1 r_0^2 (1-e^{-3})^2} exp \left(3\frac{x\sin(\alpha) + z\cos(\alpha) - f_1 r_0 \sin(\alpha)}{h_1}\right) \times \exp\left(-f_2 \frac{[x\cos(\alpha) - z\sin(\alpha) + f_1 r_0 - f_1 r_0 \cos(\alpha)]^2 + y^2}{(f_1 r_0)^2}\right) \tag{2}$$

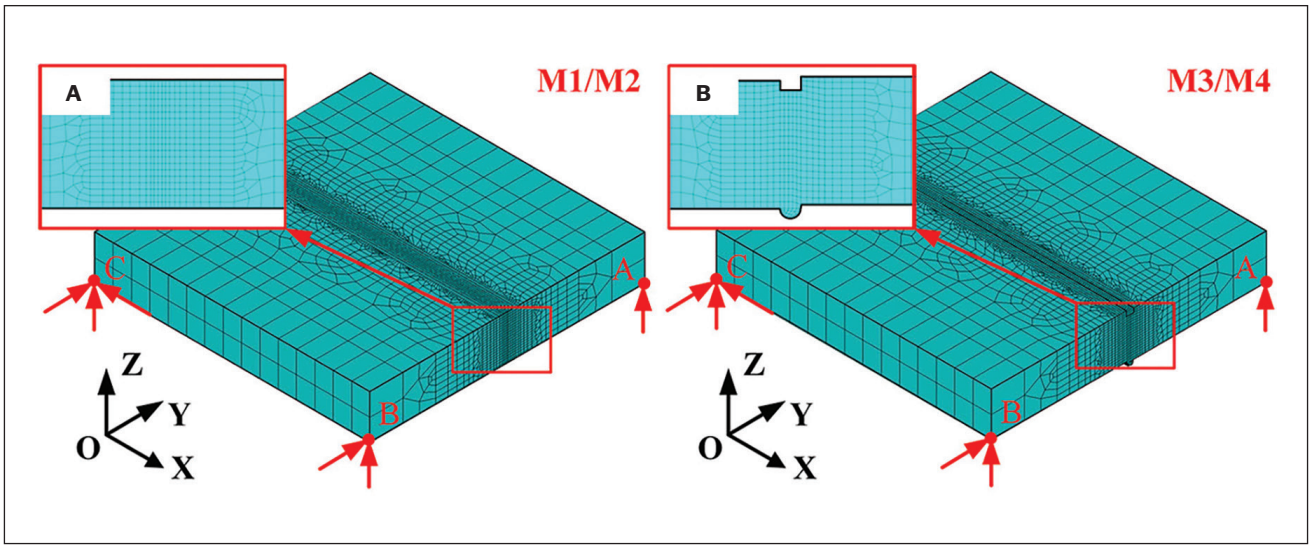


*Fig. 4 — Finite element models: A — Without weld defects (M1 and M2); B — with weld defects (M3 and M4).*

$$q_2(x,y,z) = \frac{9\lambda Q_{L2}}{\pi f_1^2 h_2 r_0^2 (1-e^{-3})^2} exp\left(-3\frac{H + x\sin(\alpha) + z\cos(\alpha) - f_1 r_0 \sin(\alpha)}{h_2}\right) \times \exp\left(-f_2 \frac{[x\cos(\alpha) - z\sin(\alpha) + f_1 r_0 - f_1 r_0 \cos(\alpha)]^2 + y^2}{(f_1 r_0)^2}\right) \quad (3)$$

where $h_1$ and $Q_{L1}$ are the height and laser power of the upper heat source, $h_2$ and $Q_{L2}$ are the height and laser power of the bottom heat source, $a$ is the heat source angle (keyhole inclining angle), $f_1$ is the radius coefficient, $f_2$ is the decay index of heat flux in thickness direction, and $H$ is the total heat source height. The initial temperature of the entire sample was 25°C (77°F). Considering the heat loss because of convection and radiation, the boundaries of the weld sample surfaces are presented as an equivalent heat transfer coefficient, $h_c$ (Ref. 17).

$$h_c = \begin{cases} 0.0668 \cdot T & W/(m^2 \cdot °C) \quad T < 500°C \\ 0.231 \cdot T - 82.1 & W/(m^2 \cdot °C) \quad T \geq 500°C \end{cases} \quad (4)$$

## Metallurgic Analysis

Based on the traditional TEP-FEM, a thermodynamic model of SSPT considering austenite transformation, ferrite and pearlite diffusion transformation, bainite transformation, and martensite transformation was developed (Refs. 18–21). During the heating and cooling process of EH40 in laser welding, austenite, ferrite and pearlite diffusion, bainite, and martensite transformation occured, respectively. The carbon equivalent $C_{eq}$ (Ref. 22) and the phase transition critical temperature of each phase was calculated by Equations 5–10, where the austenite transformation temperature was between $A_1$ and $A_3$ (Ref. 23), ferrite and pearlite diffusion transformation temperature was between $A_1$ and $B_s$, the bainite transformation temperature was between $B_s$ and $M_s$ (Ref. 24), and the martensite transformation temperature was between $M_s$ and $M_f$ (Ref. 25).

$$C_{eq} = C + \frac{Mn + Si}{6} + \frac{Cr + Mo + V}{5} + \frac{Ni + Cu}{15} \quad (5)$$

$$\begin{aligned} A_1 = {} & 723 - 7.08Mn + 37.7Si + 18.1Cr + 44.2Mo \\ & + 8.95Ni + 50.1V + 21.7Al + 3.18W \\ & + 297S - 830N - 11.5CSi - 14.0MnSi \\ & - 3.1SiCr - 57.9CMo - 5.28CNi - 15.5MnMo \\ & - 6.0MnNi + 6.77SiNi - 0.8CrNi - 27.4CV \\ & + 30.8MoV - 0.84Cr^2 - 3.46Mo^2 - 0.46Ni^2 - 28V \end{aligned} \quad (6)$$

$$\begin{aligned} A_3 = {} & 912 - 370C - 27.4Mn + 37.3Si - 6.35Cr \\ & - 32.7Ni + 95.2V + 190Ti + 72.0Al \\ & + 64.5Nb + 5.57W + 332S + 276P \\ & + 485N - 900B + 16.2CMn + 32.3CSi \\ & + 15.4CCr + 48.0CNi + 4.32SiCr - 17.3SiMo \\ & - 18.6SiNi + 4.8MnNi + 40.5MoV + 174C^2 \\ & + 2.46Mn^2 - 6.86Si^2 + 0.322Cr^2 + 9.9Mo^2 \\ & + 1.24Ni^2 - 60.2V^2 \end{aligned} \quad (7)$$

**Table 3 — Four Finite Models of EH40 Steel**

| Symbol | Unit | Value | Symbol | Unit | Value |
|---|---|---|---|---|---|
| $A_1$ | °C | 718.01 | $\Delta H_\gamma$ | J/mol | 38573 |
| $A_3$ | °C | 851.85 | $\Delta S^{xs}$ | J/mol/K | 13.48 |
| $B_s$ | °C | 642.47 | $D_c^{0\gamma}$ | m²/s | 1.5 |
| $M_s$ | °C | 401.46 | $K_1 V_{mic}$ | 1/s | $1.234 \times 10^{-4}$ |
| $M_f$ | °C | 101.46 | $K_2$ | J/mol | $2.065 \times 10^{-4}$ |
| $a_p$ | mm | $1.9 \times 10^{-3}$ | $r$ | J/mol | 2450 |
| $S_0$ | mm | $9 \times 10^{-5}$ | $p$ | / | 3.6375 |
| κ | J/K | $1.38 \times 10^{-23}$ | $\bar{x}$ | wt-% | 0.43 |
| $\omega_i$ | 1/s | $1.415 \times 10^{-13}$ | $x_s$ | wt-% | 0.03 |
| $\gamma_i$ | / | 0.45 | α | 1/K | 0.011 |
| $x_\gamma$ | / | 0.01—0.06 | | | |

$$B_s = 745 - 110C - 59Mn - 39Ni - 68Cr - 106Mo + 17MnNi + 6Cr^2 + 29Mo^2 \quad (8)$$

$$M_s = 764.2 - 302.6C - 30.6Mn - 16.6Ni - 8.9Cr + 2.4Mo - 11.3Cu + 8.58Co + 7.4W - 14.5Si \quad (9)$$

$$M_f = M_s - 300 \quad (10)$$

In the austenitization stage, the BM was transformed into austenite when the temperature increased from the starting point $A_1$ to the ending point $A_3$. According to the Johnson Mehl Avrami Kolmogorov (JMAK) theory (Refs. 20, 21), the temperature-dependent austenite fraction can be described as shown in Equation 11.

$$f_A(T) = \left[1 - \exp\left(-\frac{\pi}{3} I_A {G_A}^3 t^4\right)\right] \cdot F_A(T) \quad (11)$$

$$I_A = \frac{1.378 \times 10^{-12}}{(a_p^2 S_0)^2} \exp\left(\frac{-25.38}{T - A_1}\right) \quad (12)$$

$$G_A = \frac{7.0 \times 10^{-11}}{{S_0}^2} \exp\left(\frac{-29.70}{T - A_1}\right) \quad (13)$$

where $A$ represents austenite, $a_p$ is the edge length of the pearlite colonies, and $S_0$ is the average true interlamellar spacing.

When the EH40 weld joint was cooled to the temperature range $A_1$ and $B_s$, the austenite would undergo diffusion phase transformation due to the diffusion of atoms, transforming into ferrite and pearlite. The fraction of ferrite and pearlite could be expressed by Equation 14 (Ref. 21). Under the condition of uniform nucleation, the temperature-dependent nucleation rate expressions of ferrite and pearlite could be given by Equations 15–17 (Ref. 26).

$$f_D(T) = \left[1 - \exp\left(-\frac{\pi}{3} I_D {G_D}^3 t^4\right)\right] \cdot F_D(T) \quad (14)$$

$$I_D = C_{1i} exp\left(-\frac{Q_i}{\kappa T}\right) \cdot C_{2i} exp\left(-\frac{W_i}{\kappa T}\right) \quad (15)$$

$$C_{1i} \cdot C_{2i} = \frac{\omega_i}{\Omega} \quad (16)$$

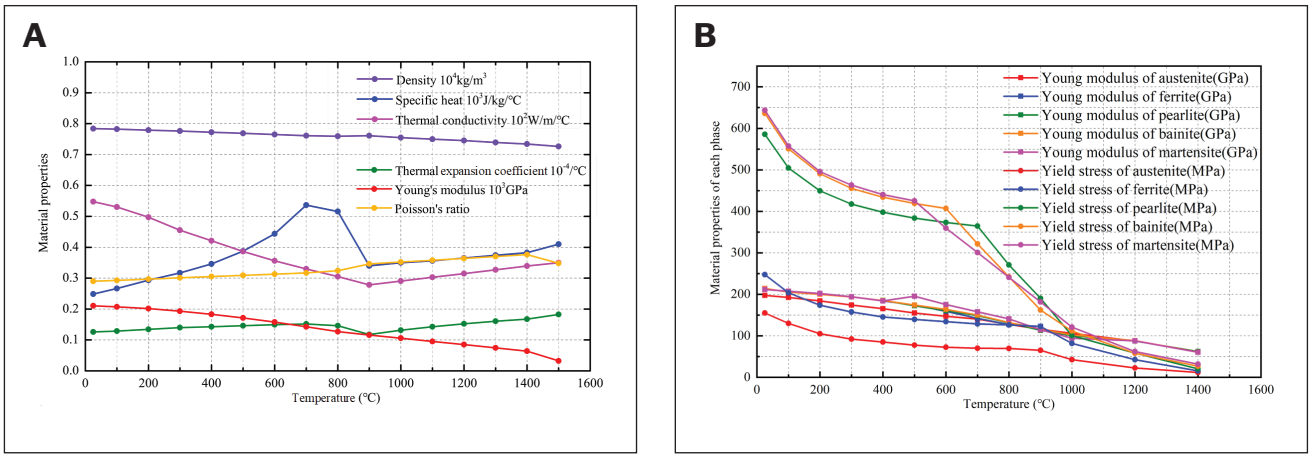


*Fig. 5 — Temperature-based material properties of: A — EH40 steel; B — each phase.*

$$W_i = \frac{16\pi\gamma_i^3}{3\left(\Delta G_i^{ch} - \Delta G_i^{\sigma}\right)^2} \tag{17}$$

where $D$ represents ferrite or pearlite, $Q_i$ is the activation energy for atomic migration per atom, $W_i$ is the change of Gibbs free energy for the critical nucleus, κ is Boltzmann's constant, and $C_{1i}$ and $C_{2i}$ are nucleation constants. $\omega_i$ is the crystal frequency, Ω is the atomic volume, $\gamma_i$ is the interfacial free energy per unit area, $\Delta G_i^{ch}$ is the volume-free energy release, and $\Delta G_i^{\sigma}$ is the strain energy. For welding, $\Delta G_i^{\sigma}$ is equal to 0, and the value of $\Delta G_i^{ch}$ can be deduced as given in Equation 18 (Ref. 27).

$$\Delta G_i^{ch} = \left\{(1-x_\gamma)\Delta G_{Fe}^{\gamma\to\alpha} + x_\gamma\left(\Delta G^{cm} - \Delta H_\gamma + \Delta S^{xs}T\right) - \frac{RT}{Z_\gamma - 1}\left[\left(1 - Z_\gamma x_\gamma\right)\ln\left(1 - Z_\gamma x_\gamma\right) - \left(1-x_\gamma\right)\ln\left(1-x_\gamma\right) + x_\gamma\left(Z_\gamma - 1\right)\ln x_\gamma\right]\right\} / 7.179/10^{-6} \tag{18}$$

where $x_\gamma$ is the carbon atom fraction in austenite, $R$ is the gas constant, $\Delta G_{Fe}^{\gamma\to\alpha}$ and $\Delta G^{cm}$ are temperature-dependent free energy, $\Delta H_\gamma$ and $\Delta S^{xs}$ are the enthalpy increment and entropy increment, respectively, and $Z_\gamma$ is an empirical parameter, which is calculated using Equation 19 (Ref. 28).

$$Z_\gamma = 14 - 12exp\left(-\frac{8054}{RT}\right) \tag{19}$$

Equation 20 expresses the growth speed under the assumption that anisotropic growth takes place during the diffusion phase transformation (Ref. 27).

$$G_i = kD_c^{0\gamma}exp\left(-\frac{Q_\gamma}{RT}\right)(T - A_1)^2 \tag{20}$$

where $k$ is a thermodynamic constant and $D_c^{0\gamma}$ is the initial diffusion coefficient of carbon in austenite.

When the temperature dropped to $B_s$ and $M_s$, the residual austenite would transform into bainite. The phase transformation thermodynamics showed that bainite formation was directly related to its nucleation rate. As shown in Equations 21–24 (Ref. 29), the increment of bainite fraction and nucleation rate are correlated linearly.

$$\dot{f}_B(T) = (1 - f_B)\cdot V_{mic}\langle\dot{N}\rangle \tag{21}$$

$$\langle\dot{N}\rangle = K_1 exp\left[-\frac{K_2}{RT}\left(1 + \frac{\langle\Delta G_{max}\rangle}{r}\right)\right] \tag{22}$$

$$\Delta G_{max} = \Delta G_{max}^0 - f_{Bmax}(\Delta G_{max}^0 - G_N) \tag{23}$$

$$G_N = pT - r \tag{24}$$

where $\dot{f}_B$ is the bainite fraction increment and $V_{mic}$ is the volume of a microregion. ⟨Ṅ⟩ denotes the nucleation rate. $K_1$, $K_2$, $p$, and $r$ are all constants. $\langle\Delta G_{max}\rangle$ is the maximum free

energy in the nucleation process, and its initial value $\Delta G^0_{max}$ can be calculated by iteratively solving Equations 25 and 26 (Ref. 30).

$$\Delta G^0_{max} = RT \ln \left| \frac{a_c^{\alpha}(x_m)}{a_c^{\gamma}(\bar{x})} \right| \tag{25}$$

$$\Delta G^{\gamma \to \alpha}_{Fe} + RT \ln \left| \frac{a_{Fe}^{\alpha}(1-x)}{a_{Fe}^{\gamma}(1-\bar{x})} \right| - RT \ln \left| \frac{a_c^{\alpha}(x)}{a_c^{\gamma}(\bar{x})} \right| = 0 \tag{26}$$

where $a_{Fe}$ and $a_c$ are the activities of iron and carbon, respectively; γ and α present austenite and ferrite, respectively; $\bar{x}$ is the average carbon concentration; and $x_m$ is the carbon concentration obtained by equilibrium iteration of Equation 26.

When the weld joint was cooled to a temperature between $M_s$ and $M_f$, the residual austenite would transform into martensite. Based on the assumption that the fractional increment is linear to the temperature rise (Ref. 31), Equation 27 determined the martensite fraction.

$$f_M(T) = 1 - exp[-\alpha(M_s - T)] \tag{27}$$

where $f_M$ is the martensite fraction and α is an empirical coefficient.

Due to the strong correlation between hardness and the microstructure of welded joints, hardness is widely used in the validation of the SSPT model. The Maynier model is usually used to predict the hardness distribution (Ref. 22). According to the rules for calculating the mixed-phase properties, the hardness can be calculated by the following equation:

$$H_v = H_F \cdot f_F + H_B \cdot f_B + H_M \cdot f_M + H_{bm} \cdot f_{bm} \tag{28}$$

where $H_F$, $H_B$, $H_M$, and $H_{bm}$ are the hardness of ferrite, bainite, martensite, and BM, respectively; $f_F$, $f_B$, $f_M$, and $f_{bm}$ are the fraction of ferrite, bainite, martensite, and BM, respectively. In addition, $H_F$, $H_B$, and $H_M$ are all related to the cooling rate, Equations 29–31.

$$\begin{aligned} H_F = {} & 42 + 223w(C) + 53w(Si) + 30w(Mn) \\ & + 12.6w(Ni) + 7w(Cr) + 19w(Mo) \\ & + lgv[10 - 19w(C) + 4w(Si) + 8w(Cr) - 33w(V)] \end{aligned} \tag{29}$$

$$\begin{aligned} H_B = {} & -323 + 185w(C) + 330w(Si) + 153w(Mn) \\ & + 65w(Ni) + 144w(Cr) + 191w(Mo) \\ & + lgv\begin{bmatrix} 89 + 53w(C) - 55w(Si) - 22w(Mn) \\ - 10w(Ni) - 20w(Cr) - 33w(Mo) \end{bmatrix} \end{aligned} \tag{30}$$

$$\begin{aligned} H_M = {} & 127 + 949w(C) + 27w(Si) \\ & + 11w(Mn) + 8w(Ni) + 16w(Cr) + 21lgv \end{aligned} \tag{31}$$

where $v$ is the cooling rate at 700°C (1292°F) during the cooling process and $w(x)$ is the content of element $x$.

## Mechanical Analysis

SSPT has a great impact on welding residual stress. Thereby, the total strain increment can be described by Equation 32.

$$d\varepsilon_{total} = d\varepsilon_e + d\varepsilon_p + d\varepsilon_T + d\varepsilon_{vol} + d\varepsilon_{tp} \tag{32}$$

where $d\varepsilon_{total}$ is total strain increment, $d\varepsilon_e$ is elastic strain increment, $d\varepsilon_p$ is plastic strain increment, $d\varepsilon_T$ is temperature strain increment, $d\varepsilon_{vol}$ is transformation-induced volume increment, and $d\varepsilon_{tp}$ is transformation-induced plasticity increment. Computations of them were all related to material properties under different temperatures, as shown in Fig. 5. The transformation-induced increment ($d\varepsilon_{vol}$ and $d\varepsilon_{tp}$) was the basis of the welding mechanics calculation considering the effect of SSPT. The calculation equations of $d\varepsilon_{vol}$ and $d\varepsilon_{tp}$ are as follows:

$$\begin{aligned} d\varepsilon_{vol} = {} & \boldsymbol{B}\left( \sqrt[3]{1 - f_{new} + f_{new}\frac{V_{new}}{V_{old}}} - 1 \right) \\ & d\boldsymbol{u} - \alpha(1 - f_M) \cdot dT \cdot d\varepsilon_{volM} \end{aligned} \tag{33}$$

$$d\varepsilon_{tp} = 3K(1 - f_M) \cdot df_M \cdot s_{ij} \tag{34}$$

where $\boldsymbol{B}$ is the displacement-strain matrix and $d\boldsymbol{u}$ is the increment of each element displacement, $f_{new}$ is the sum of the fraction of the production microstructures, $V_{new}$ and $V_{old}$ are the atom volumes of the production phase and parent phase, respectively, $f_M$ and $df_M$ are the fractions of martensite and its increment, respectively, $dT$ is the temperature difference, $d\varepsilon_{volM}$ is the volume strain with the full martensite transformation, $s_{ij}$ is the stress deviator, and $K$ is the coefficient of the transformation plasticity. In addition, points A, B, and C were constrained to prevent the rigid body motion of the sample, as shown in Fig. 4.

Meanwhile, Table 3 provides a summary and list of the symbols and values in the proposed FEM integrated with thermodynamics-based solid phase transformation.

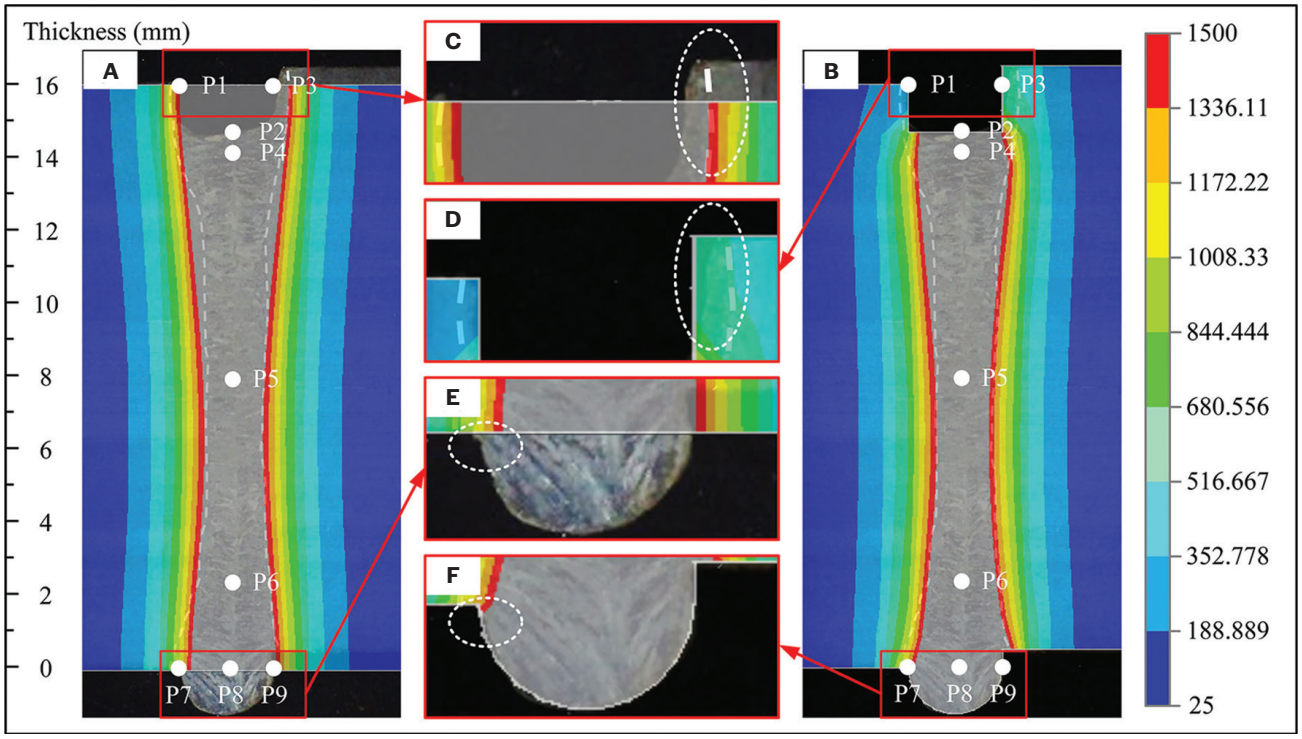


*Fig. 6 — Comparison of the experimentally measured and numerically predicted weld bead cross sections of: A — M1; B — M3. C–F is the magnification of the weld bead cross section top and bottom of M1 and M3.*

## Results and Discussion

### Validation of Thermal Model

In the thermal analysis, only the weld defects (collapse, hump, and unfitness) were considered, thus M1 and M2 had the same temperature distributions and so did the distributions of M3 and M4. In Fig. 6, the temperature distributions of M1/M2 and M3/M4 were overlaid onto the corresponding weld cross section. The FZ, featured by the grey area, had a peak temperature higher than or equal to the melting temperature of the BM (1500°C [2732°F]). These two thermal models both achieved excellent prediction in the temperature distribution. The simulation errors of the thermal simulation were calculated by the average error between the simulated and the actual weld width in the direction of plate thickness. The simulation errors of M1/M2 and M3/M4 through the thickness were 9.2 and 3.5%, respectively.

However, there were obvious differences in the temperature distribution between M1/M2 and M3/M4 despite the same heat source model, especially in the zones near the weld defects. The upper width of the FZ of M1/M2 was larger than that of M3/M4, while the bottom width was smaller, as shown in Figs. 6E and F. The transient temperature processes of nine points (P1–P9 were marked in Figs. 6A and B) were obtained to further investigate the effect of weld defects on the thermal cycles in the joint, as shown in Fig. 7. The weld defects on the thermal cycles of P3, P9, P1, and P7 were largest (the variations of their peak temperatures were 1541.1°C [2806°F], 1221.4°C [2230.5°F], 1050.6°C [1923.1°F], and 562.4°C [1044.3°F]) followed by that of P8, P4, P2, and P6 (the variations of their peak temperatures were 338.9°C [642°F], 304.2°C [579.6°F], 193°C [379.4°F], and 164°C [327.2°F]), whereas that of P5 was hardly affected. It indicated that the weld defects mainly affected the thermal cycles in the vicinity, and the influence decreased with the distance from the weld defects. The loss of metal material caused by collapse blocked the energy conduction to the surrounding area, contributing to a lower weld width at the top of the weld and a higher local peak temperature. On the contrary, the hump conducted energy easily to the surrounding area, resulting in a bigger weld width at the bottom of the weld and a lower local peak temperature. Thereby, the peak temperatures of P1–P4 with collapse were higher, while the peak temperatures of P1–P4 with hump were lower as was the temperature change rate.

**Table 4 — The Maximum Value of Each Phase**

| | Base Metal | Ferrite | Bainite | Martensite |
|---|---|---|---|---|
| M2 | 1 | 1 | 0.000823 | 0.999611 |
| M4 | 1 | 1 | 0.000818 | 0.999687 |

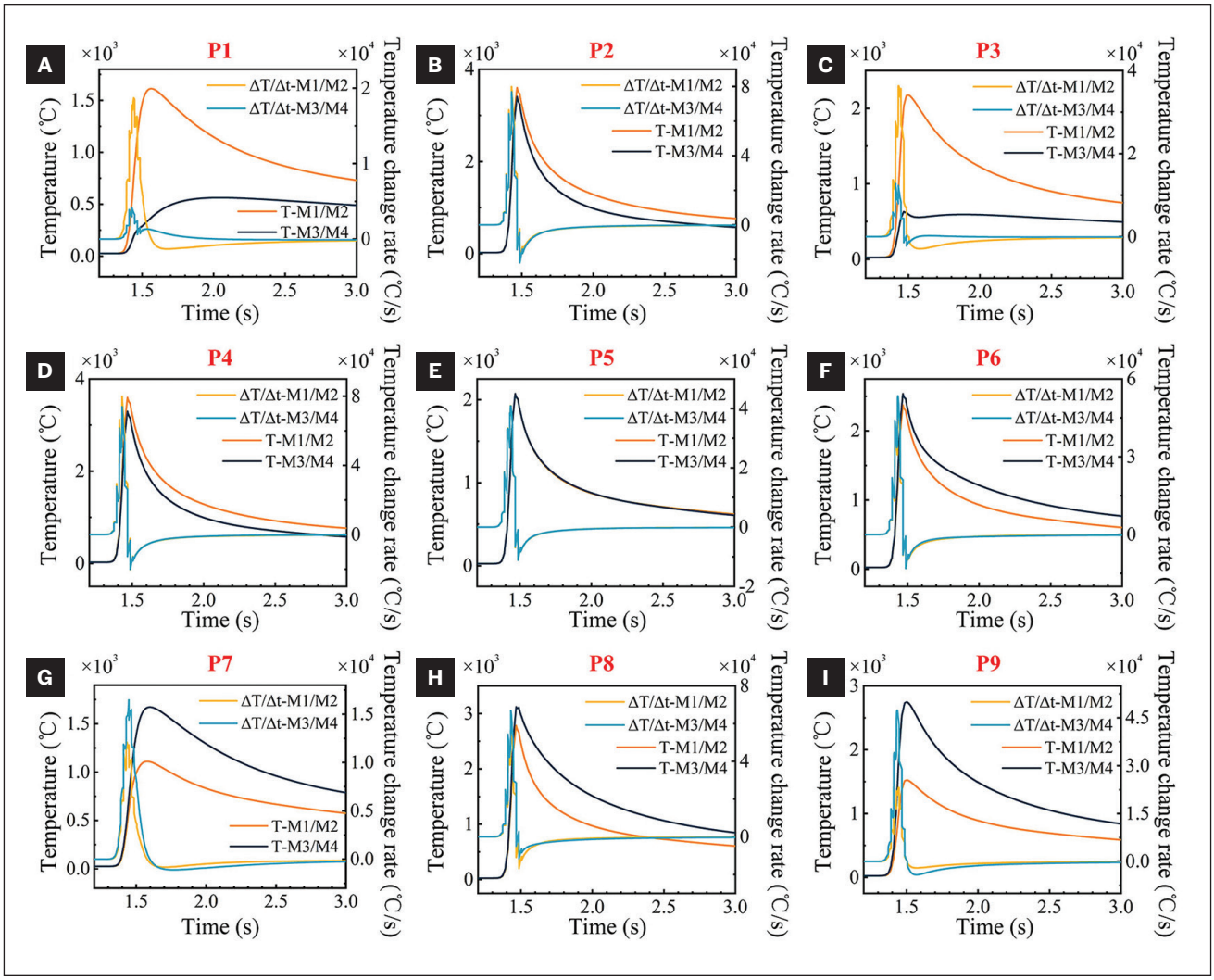


*Fig. 7 — Transient temperature analysis at: A — P1; B — P2; C — P3; D — P4; E — P5; F — P6; G — P7; H — P8; I — P9.*

## Validation of SSPT Model

Based on the SSPT model, the fractions of the BM, ferrite, bainite, and martensite were calculated. The final distributions of phase fractions in M2 and M4 are shown in Fig. 8, while the maximum value of each phase is given in Table 4. The results show that SSPT is concentrated near the FZ and inhomogeneous in the welding direction. The peak fraction of martensite was located at the start-welding zone, while that of ferrite appeared at the end-welding zone. And there was almost no bainite in the weld. These were attributed to differences in the cooling rate: The cooling rate at the start-welding zone was higher, and martensite was more easily formed at a high cooling rate.

Furthermore, the fractions of each phase in M2 and M4 were different, especially near the weld defects. At the end-welding zone, M2 had more ferrite at the top and more martensite at the bottom. As mentioned above, this was attributed to the thermal cycle; thermodynamics served as the foundation for the SSPT model. The collapse decreased the peak temperature and cooling rate in its vicinity, and the hump had the opposite effect. So, more martensite formed at the bottom of M2 and the top of M4 because of the high cooling rate.

To verify the validity of the SSPT model, the simulation and actual distributions of phases were compared. Figure 9 shows the simulated phase distributions of the metallographic detection location. Martensite transformation was the main phase transformation in the weld joint. The microstructure of the FZ was martensite, and as the distance from the weld center increased, martensite reduced while ferrite (the BM's microstructure) increased, which showed good agreement with the experimental distributions shown in Fig. 3. Moreover, due to the strong correlation between hardness and microstructure, hardness is widely used in SSPT model verification. So, the hardness distributions along Lines A, B, and C of simulation and test were compared in Fig. 10. The hardness of different positions in the thickness direction had similar distribution law: The hardness near the weld center was obviously higher than that far away from the weld center. This was consistent with microstructure distribution; martensite with high hardness was the main phase in the FZ. In

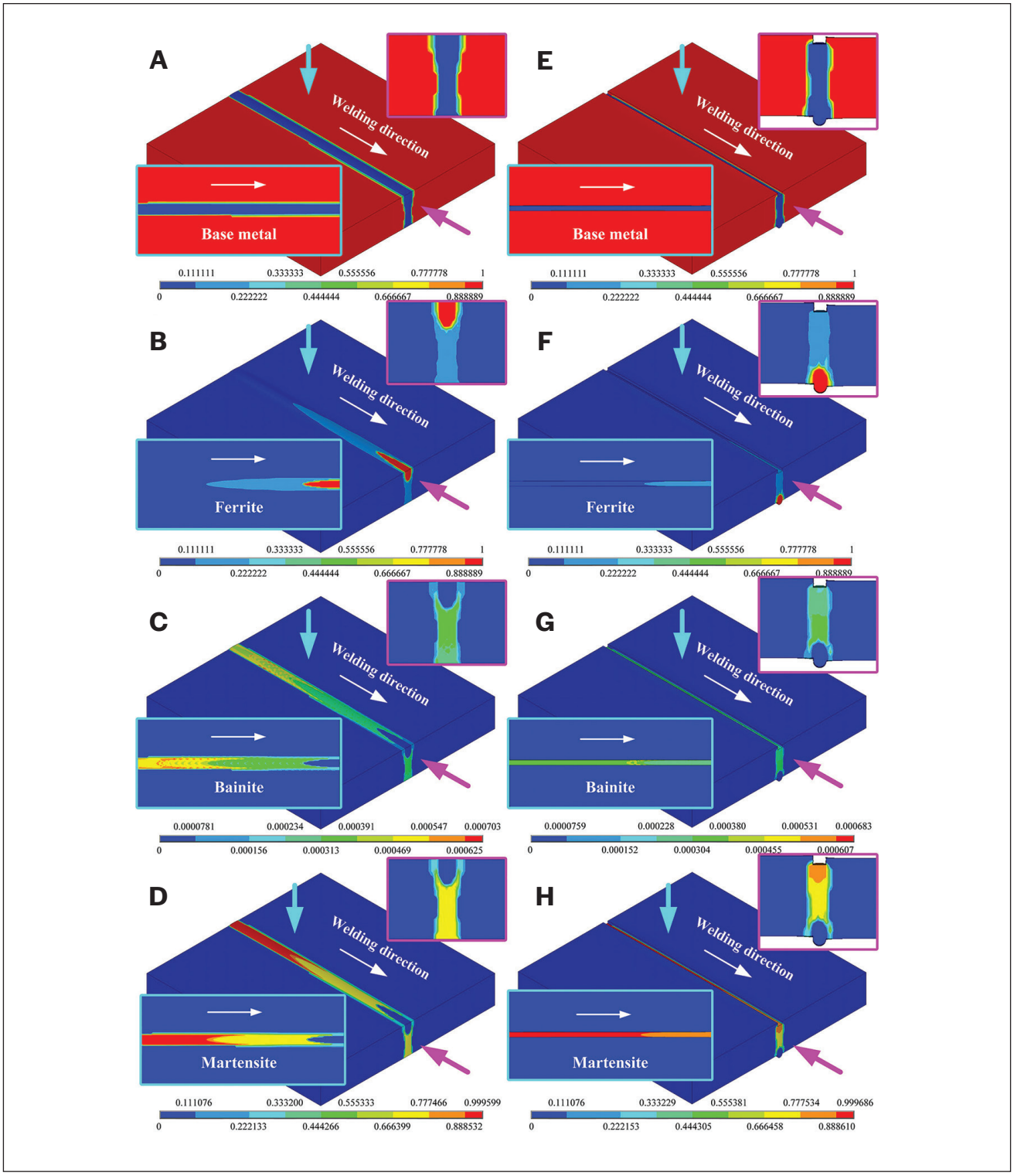


*Fig. 8 — The final fraction: A — Base metal; B — ferrite; C — bainite; D — martensite in M2. The fraction of: E — base metal; F — ferrite; G — bainite; H — martensite in M4.*

addition, when weld defects were considered, the hardness prediction matched better with the experimental results due to the better accuracy of the temperature distribution. The errors between M4 and the test of hardness along Lines A, B, and C were within 100 HV, proving the validity of the SSPT model. The error may have been caused by the release of residual stress from cutting and polishing because the residual stress has an influence on the hardness (Ref. 32). In addition, the Maynier model was built based on multiple regression analyses of the cooling transition curve, and the

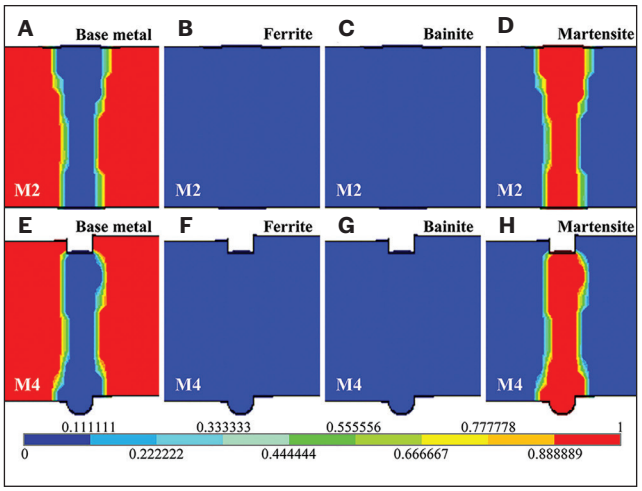


*Fig. 9 — A — Base metal; B — ferrite; C — bainite; D — martensite distributions of the metallographic detection location in M2. E — Base metal; F — ferrite; G — bainite; H — martensite distributions of the metallographic detection location in M4.*

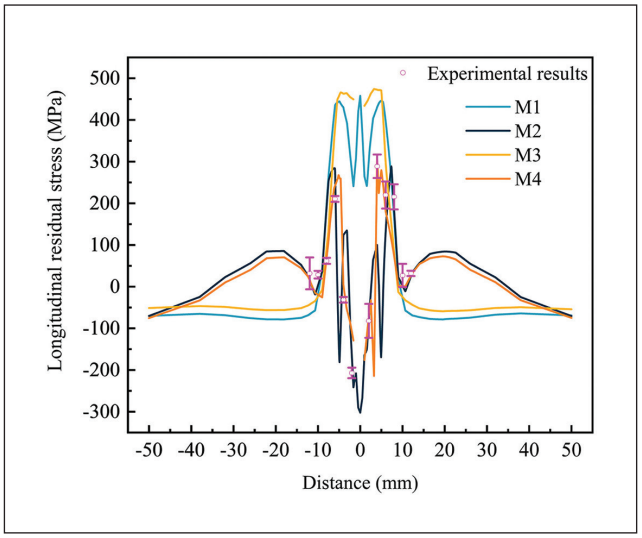


*Fig. 11 — Comparison of experimental and numerical longitudinal residual stress along Line 1 (marked in Fig. 2).*

influences of grain size (Refs. 33, 34), dislocation density (Refs. 35, 36), and plastic strain (Refs. 14, 37–39) on hardness were not fully considered, which limits the scope of application.

## Residual Stress Distribution

The LRS along Line 1 is shown in Fig. 11 and Table 5, including the results of simulation and test results. The reliability and accuracy of the models were further illustrated by the good agreement between the simulation results and the experimental results. A better prediction was obtained when the SSPT was considered (M3 and M4). Meanwhile, compressive stress appeared and high tensile stress disappeared in

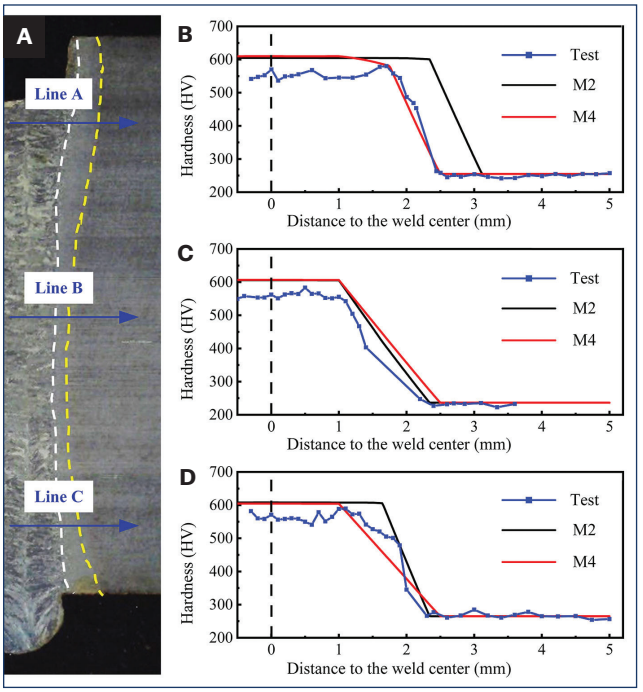


*Fig. 10 — A — The schematic diagram of hardness test position. The hardness distribution of simulation and test: B — Along Line A; C — along Line B; D — along Line C.*

the weld center zone. For the upper surface of the welded joint, the influence of weld defects mainly showed in the weld center zone, which was the high-stress zone (≥ 100 MPa) and where the weld defects were located. The maximum variation of LRS between M1 and M3 was 208.27 MPa, and that between M2 and M4 was 445.13 MPa. It can be concluded that the weld defects have an important influence on the value of LRS, and this influence is magnified by SSPT. In addition, the widths of the high-stress zones of M1–M4 were 14.4 (0.57), 9.05 (0.35), 13.1 (0.52), and 9 mm (0.35 in.). When weld defects were considered, the high-stress zone had a smaller width. This means that the weld defects affected the distribution of LRS. Thus, when simulating thick-plate laser welding, weld defects and SSPT should both be considered.

To study the inhomogeneous stress distribution of thick-plate EH40 joints in single-pass complete joint penetration laser welding, four data curves (Line A, Line B, and Line C) of the welded joint were extracted in Fig. 12. The variations of LRS in the upper, mid, and lower parts of the welded joint are shown in Figs. 12A–C. Firstly, it is obvious that the distribution of LRS in both the thickness direction and the width direction was inhomogeneous. Take M4 as an example. The stress fluctuations along Line A, Line B, and Line C were 533.89, 620.88, and 493.92 MPa. Moreover, the distribution rules of LRS along Lines A–C were similar: The stress near the FZ was high, and the stress far away from the FZ was low, which is deeply related to the inhomogeneous heat input during the high-power laser welding. Further, comparing the LRS of models with and without SSPT, it was found that the effect of SSPT was obvious and made LRS along these three lines all compressive near the FZ. From the above, the microstructure

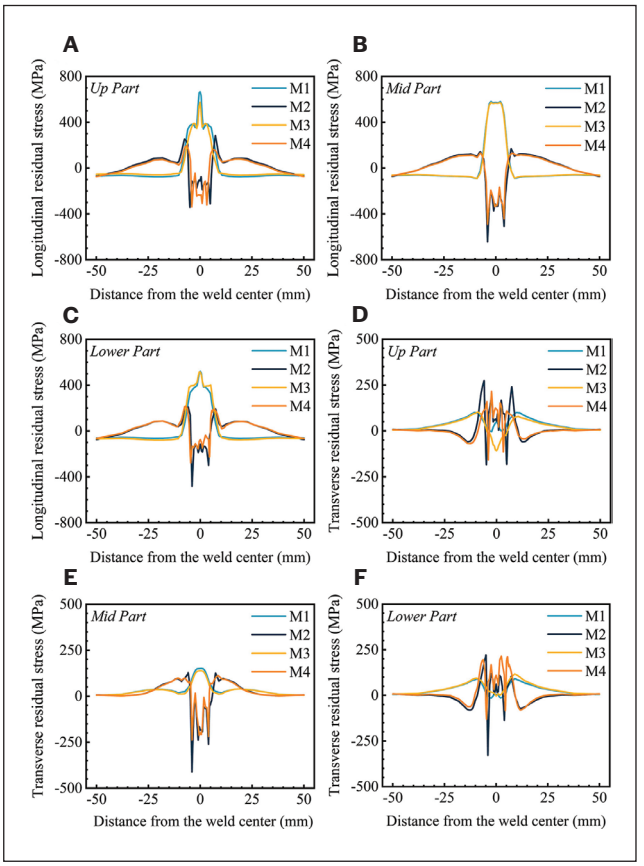


*Fig. 12 — The longitudinal residual stress variations: A — In the upper part; B — in the mid part; C — in the lower part. The transverse residual stress variations: D — in the upper part; E — in the mid part; F — in the lower part.*

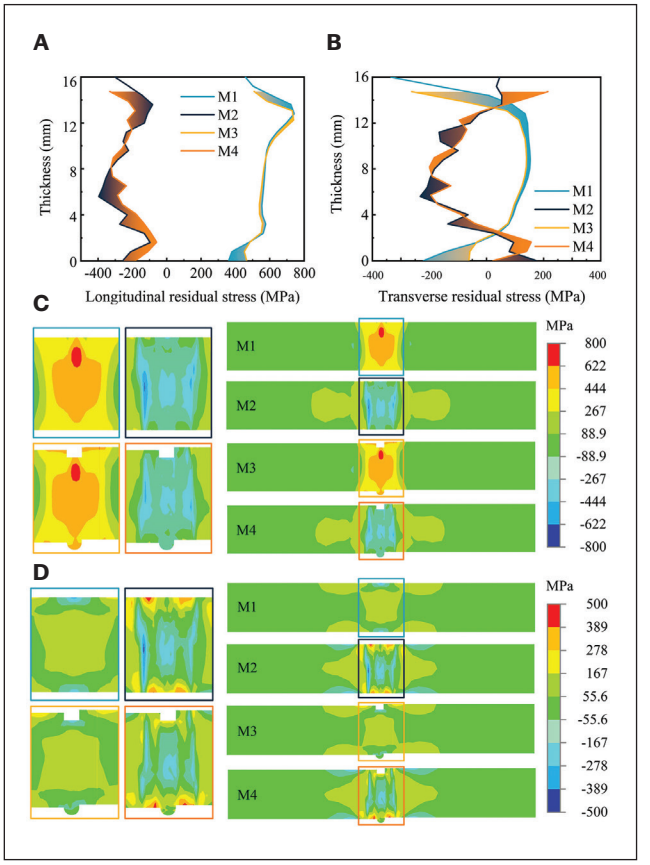


*Fig. 13 — A — The longitudinal residual stress; B — the transverse residual stress variations through thickness of welded joint. C — The LRS contour; D — the transverse residual stress contour in M1, M2, M3, and M4.*

of the FZ was almost all martensite. This means that martensite transformation played the main role in the distribution of LRS. In other words, the shear volumetric strain and induced plasticity strain caused by martensite transformation were the main reasons for the formation of compressive stress in the FZ. In addition, it was found that the weld defects had an influence on the value of residual stress, and this effect was greater when SSPT was considered. For LRS along Line A, the maximum variations of the model without and with SSPT were 153.29 and 434.53 MPa, and that along Lines B and C were 45.27, 159.32, 92.3, and 350.63 MPa, respectively. Meanwhile, LRS in zones with metal loss/increase or sharp geometry changes caused by weld defects were more susceptible. The effect of weld defects on LRS along Lines A and C was larger than that along Line B.

Different from LRS, the effect of SSPT on TRS was more complicated. For the upper part of the welded joint, one more compression-tension stress transition occured near the FZ (in M2 and M4) due to SSPT, as shown in Fig. 12D. The peak and the fluctuation range of TRS increased by approximately two times: The TRS peaks of M1–M4 were 99.84, 273.34, –107.65, and 215.74 MPa, while the TRS fluctuation ranges of M1–M4 were 103.38, 457.48, 209.54, and 373.98 MPa. For the mid part of the welded joint, the effect of SSPT on TRS was similar to that on LRS; TRS was compressive near the FZ. SSPT resulted in more-frequent stress fluctuation, a larger stress peak, and a bigger stress fluctuation range in the lower part of the welded joint. Similar to the LRS, the TRS in the upper and lower parts of the welded joint was more easily affected by weld defects. The collapse reduced the value of TRS along Line A significantly, and the hump increased that along Line C, as shown in Figs. 12D and F. Weld defects had little influence on the TRS in the mid part of the welded joint.

To further investigate the effect of weld defects and SSPT on the residual stress distribution, LRS and TRS data cavers along path Line 2 and the stress nephogram on the mid-plane section of the welded joint were extracted in Fig. 13. When only weld defects were considered, these mainly affected LRS in their vicinity: the upper and lower parts of the welded joint, while the mid part of that is almost unaffected. However, when SSPT was considered, the weld defects affected the LRS of the entire welded joint. The maximum variation of LRS between the model with and without the weld defects (M4 and M2) exceeded 150 MPa. When SSPT was not considered, the variations of LRS between the model with and without the weld defects (M3 and M1) were within 100 MPa. This means that the effect of the weld defects on LRS was amplified by SSPT. It can be found that weld defects have similar effects

**Table 5 — The Residual Stress Error between the Simulation Results and the Experimental Results**

| Distance from the Weld Center (mm) | Experimental Results (MPa) | M1 | M2 | M3 | M4 |
|---|---|---|---|---|---|
| | | | Absolute Error (MPa) | | |
| –12 | 39.48 ± 5.77 | –105.74 | –22.72 | –82.45 | –23.42 |
| –10 | 28.89 ± 9.11 | –47.60 | –26.04 | –52.75 | –48.21 |
| –8 | 62.06 ± 7.33 | 128.71 | 121.80 | 26.22 | 2.95 |
| –6 | 210.60 ± 7.00 | 220.92 | 73.27 | 165.20 | 30.38 |
| –4 | –31.45 ± 6.76 | 461.82 | 155.09 | 494.26 | 36.81 |
| –2 | –204.28 ± 10.62 | 484.15 | 42.85 | 656.53 | 97.43 |
| 2 | –81.85 ± 40.79 | 380.65 | –5.77 | 533.72 | 5.88 |
| 4 | 288.83 ± 28.13 | 141.46 | –188.95 | 183.83 | 21.49 |
| 6 | 220.01 ± 32.48 | 179.12 | –93.61 | 81.84 | –37.93 |
| 8 | 215.59 ± 30.06 | –48.47 | –28.11 | –129.32 | –140.92 |
| 10 | 27.02 ± 27.88 | –53.74 | –24.60 | –51.72 | –25.67 |
| 12 | 31.95 ± 6.35 | –98.59 | –6.99 | –73.32 | –5.61 |
| Average error (MPa) | | 136.89 | –0.32 | 146.00 | –7.24 |
| Maximum error (MPa) | | 484.15 | –188.95 | 656.53 | –140.92 |

on LRS and TRS, and the latter is greater, as shown in Figs. 13A and B. The weld defects resulted in a maximum variation of TRS above 150 MPa. Take the thickness of 0 mm as an example. The variations of LRS and TRS between M3 and M1 were 105.63 and 159.80 MPa, while those between M4 and M2 were 71.91 and 153.50 MPa. Under the action of SSPT, the properties of each zone of the welded joint varied significantly, and the inhomogeneity of expansion and contraction behavior in the welded joint intensified. The influence of the loss and increase of metal on the LRS and TRS became greater. Moreover, the affected zone extended from the vicinity of weld defects to the whole. In addition, the weld defects were simplified in the welding direction (i.e., the direction of LRS), and the geometry size of the weld defects did not change. Therefore, stress concentration had little influence on LRS. However, for TRS, the weld defects caused sharp geometry changes, and the stress concentration became obvious. So, weld defects had a greater influence on the TRS.

## Residual Stress Evolution Analysis

The evolution processes of residual stress in different points of the welded joint were extracted to investigate the effect mechanism of weld defects on the thermal-metallurgical-mechanical behavior in laser keyhole welding of EH40 steel, as shown in Figs. 14–16. For the upper part of the welded joint (P1–P3), the weld defects affected the final value of LRS, and TRS had a greater effect on TRS. The fluctuation of P3 TRS reached 225.77 MPa after considering weld defects. The fluctuation trends of the LRS of different nodes were not affected by the weld defects. However, the TRS of P1 and P3 were changed, obviously: The fluctuation range of the TRS of P1 was smaller, and the tension of the TRS of P3 was suppressed and finally formed compressive stress. For the lower part of the welded joint, weld defects had a similar effect on residual stress of the upper part of the welded joint, but the fluctuation range of TRS with weld defects was bigger. Compared to the residual stress evolution process of P4, P5, and P6 along the thickness direction, it can be found that weld defects have little influence on LRS and TRS

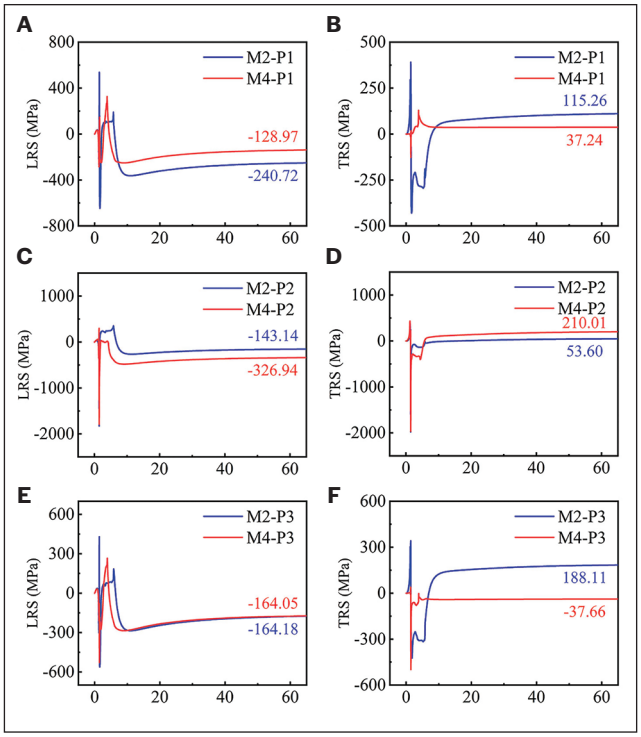


*Fig. 14 — Stress time-dependent curves of nodes in M2 and M4: A, C, E — LRS of P1, P2, and P3; B, D, F — TRS of P1, P2, and P3.*

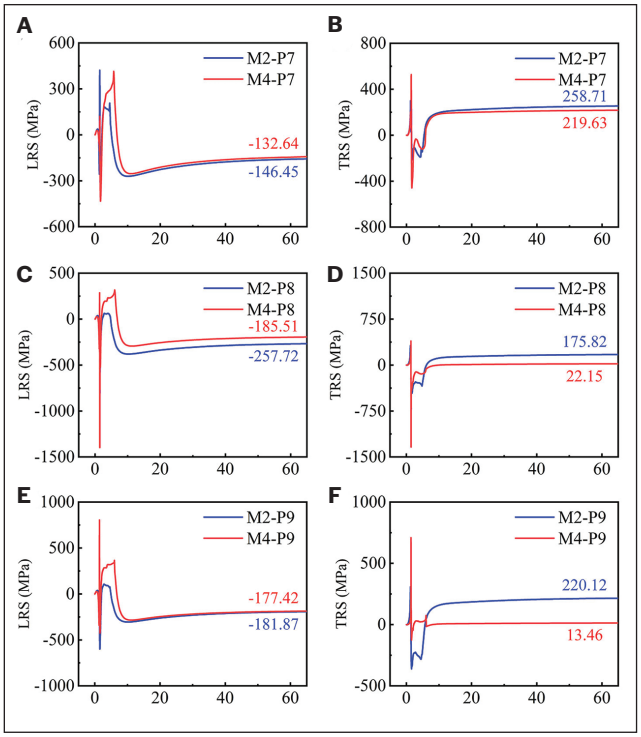


*Fig. 15 — Stress time-dependent curves of nodes in M2 and M4: A, C, E — LRS of P7, P8, and P9; B, D, F — TRS of P7, P8, and P9.*

in the mid part of the welded joint. It can be concluded that weld defects mainly affect the thermal-metallurgical-mechanical behavior in the collapse and hump zones, which is deeply correlated with the loss and increase of metal and the stress concentration caused by shape geometry changes. The interaction with the surrounding metal was reduced by the loss of metal, resulting in a flatter stress evolution curve, as shown in Fig. 14. On the contrary, after considering weld defects, due to the increase of nearby metal, the LRS and TRS of three points (P7–P9) in the lower part of the welded joint fluctuated more violently in the evolution process, as shown in Fig. 15. Stress concentration can enhance or weaken the stress, which is related to the stress state of the point.

## Conclusions

In this paper, the effects of weld defects and SSPT on residual stress of marine steel EH40 with a thickness of 16 mm in high-power laser welding were analyzed. The thermal-metallurgical-mechanical theory was used to investigate the thermal field, distribution of microstructure, and residual stress. The following conclusions are summarized:

1) The weld geometry was fitted well by a double-cylindrical source model. The mean prediction errors of the model without and with weld defects along the distribution of thickness were 9.2 and 3.5%. To guarantee the residual stress prediction validity, microstructure fractions were computed and verified by hardness test results based on the thermodynamics of SSPT. The errors between M4 (with weld defects and

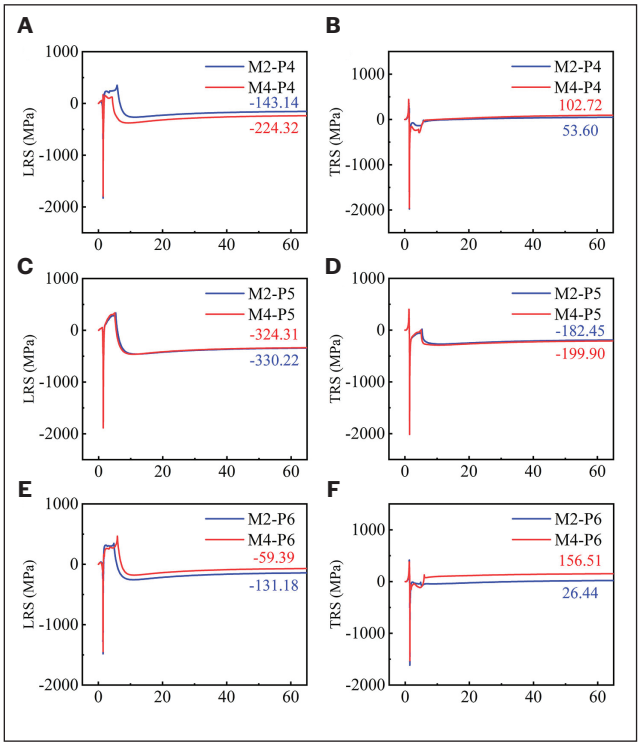


*Fig. 16 — Stress time-dependent curves of nodes in M2 and M4: A, C, E — LRS of P4, P5, and P6; B, D, F — TRS of P4, P5, and P6.*

SSPT) and the test of hardness with different thicknesses were all within 100 HV, proving the validity of the SSPT model.

2) Under the effect of SSPT, residual stress changed from compressive stress to tensile stress with the increase of the distance from the weld center. This is closely related to the expansion and extrusion caused by martensite transformation in the FZ, which cancels the tensile stress near the martensite.

3) The weld defects affected the value of residual stress, and this influence was greater under the effect of SSPT. When SSPT was not considered, the weld defects mainly affected the residual stress in their vicinity. When SSPT was considered, the residual stress of the whole weld was affected by weld defects, and the variation of both LRS and TRS along the plate thickness exceeded 150 MPa.

4) Compared to the residual stress distribution of welded joints and the evolution process of nodes, it was found that the loss and increase of metal caused by weld defects and the stress concentration caused by shape geometry changes were the main influencing mechanisms of weld defects on residual stress. In addition, the influence of weld defects on TRS was greater than that on LRS because the stress concentration caused by shape geometry changes has little influence on LRS.

## Acknowledgment

This research is funded by the National Natural Science Foundation of China (51905191 and 52188102) and the Postdoctoral Science Foundation of China (2021M691113). The general characterization facilities were provided by the Flexible Electronics Manufacturing Laboratory in the Experiment Center for Advanced Manufacturing and Technology in the School of Mechanical Science & Engineering of Huazhong University of Science and Technology.

## References

1. Zhang, M., Liu, T., Hu, R., Mu, Z., Chen, S., and Chen, G. 2020. Understanding root humping in high-power laser welding of stainless steels: A combination approach. *International Journal of Advanced Manufacturing Technology* 106(11–12): 5353–5364. DOI: 10.1007/s00170-020-05021-6

2. Meng, W., Xu, Z., Ma, Q., Yin, X., and Fang, J. 2019. Pulse fiber laser welding of AISI 321-AISI 405 stainless steel thick plates butt joints. *Journal of Materials Processing Technology* 271(March): 214–225. DOI: 10.1016/j.jmatprotec.2019.04.013

3. Jiang, M., Jiang, N., Chen, X., Ma, S., Chen, Y., Chen, Y., et al. 2021. Experimental and numerical investigation of single-pass laser welding of 20 mm-thick high-strength steel under reduced ambient pressure. *Journal of Materials Research and Technology* 15: 2317–2331. DOI: 10.1016/j.jmrt.2021.09.030

4. Kawahito, Y., Wang, H., Katayama, S., and Sumimori, D. 2018. Ultra high power (100 kW) fiber laser welding of steel. *Optics Letters* 43(19): 4667. DOI: 10.1364/OL.43.004667

5. Yang, X., Yan, G., Xiu, Y., Yang, Z., Wang, G., Liu, W., et al. 2019. Welding temperature distribution and residual stresses in thick welded plates of SA738Gr.B through experimental measurements and finite element analysis. *Materials* 12(15): 2436. DOI: 10.3390/ma12152436

6. Banik, S. D., Kumar, S., Singh, P. K., Bhattacharya, S., and Mahapatra, M. M. 2021. Distortion and residual stresses in thick plate weld joint of austenitic stainless steel: Experiments and analysis. *Journal of Materials Processing Technology* 289: 116944. DOI: 10.1016/j.jmatprotec.2020.116944

7. Ibrahim, O. A., Lignos, D. G., and Rogers, C. A. 2019. Recommendations for improved welding procedures for thick steel plates through thermo-mechanical analysis. *International Journal of Steel Structures* 19(1): 193–212. DOI: 10.1007/s13296-018-0110-2

8. Xu, G., Pan, H., Liu, P., Li, P., Hu, Q., and Du, B. 2018. Finite element analysis of residual stress in hybrid laser-arc welding for butt joint of 12 mm-thick steel plate. *Welding in the World* 62(2): 289–300. DOI: 10.1007/s40194-017-0545-7

9. Zhang, H., Jiang, M., Chen, X., Wei, L., Wang, S., Jiang, Y., et al. 2022. Investigation of weld root defects in high-power full-penetration laser welding of high-strength steel. *Materials* 15(3): 1095. DOI: 10.3390/ma15031095

10. Bunaziv, I., Dørum, C., Nielsen, S. E., Suikkanen, P., Ren, X., Nyhus, B., et al. 2021. Root formation and metallurgical challenges in laser beam and laser-arc hybrid welding of thick structural steel. *International Journal of Advanced Manufacturing Technology* 116 (1–2): 561–578. DOI: 10.1007/s00170-021-07453-0

11. Rong, Y., Xu, J., Lei, T., Wang, W., Sabbar, A. A., Huang, Y., et al. 2018. Microstructure and alloy element distribution of dissimilar joint 316L and EH36 in laser welding. *Science and Technology of Welding and Joining* 23(6): 454–461. DOI: 10.1080/13621718.2017.1410342

12. Liang, R., Luo, Y., and Li, Z. 2018. The effect of humping on residual stress and distortion in high-speed laser welding using coupled CFD-FEM model. *Optics and Laser Technology* 104: 201–205. DOI: 10.1016/j.optlastec.2018.02.024

13. Xia, J., and Jin, H. 2017. Numerical study of welding simulation and residual stress on butt welding of dissimilar thickness of austenitic stainless steel. *International Journal of Advanced Manufacturing Technology* 91: 227–235. DOI: 10.1007/s00170-016-9738-2

14. Tiryakioğlu, M. 2015. On the relationship between Vickers hardness and yield stress in Al-Zn-Mg-Cu Alloys. *Materials Science and Engineering A* 633: 17–19. DOI: 10.1016/j.msea.2015.02.073

15. Mi, G., Wei, Y., Zhan, X., Gu, C., and Yu, F. 2014. A coupled thermal and metallurgical model for welding simulation of Ti–6Al–4V alloy. *Journal of Materials Processing Technology* 214(11): 2434–2443. DOI: 10.1016/j.jmatprotec.2014.05.011

16. Rong, Y., Wang, L., Wu, R., and Xu, J. 2022. Visualization and simulation of 1700MS sheet laser welding based on three-dimensional geometries of weld pool and keyhole. *International Journal of Thermal Sciences* 171: 107257. DOI: 10.1016/j.ijthermalsci.2021.107257

17. Brickstad, B., and Josefson, B. L. 1998. A parametric study of residual stresses in multi-pass butt-welded stainless steel pipes. *International Journal of Pressure Vessels and Piping* 75(1): 11–25.

18. Wang, H., Woo, W., Kim, D. K., Em, V., and Lee, S. Y. 2018. Effect of chemical dilution and the number of weld layers on residual stresses in a multi-pass low-transformation-temperature weld. *Materials and Design* 160: 384–394.

19. Rong, Y., Lei, T., Xu, J., Huang, Y., and Wang, C. 2018. Residual stress modelling in laser welding marine steel EH36 considering a thermodynamics-based solid phase transformation. *International Journal of Mechanical Sciences* 146–147: 180–190. DOI: 10.1016/j.ijmecsci.2018.07.046

20. Moghadam, M. M., and Voorhees, P. W. 2016. Thin film phase transformation kinetics: From theory to experiment. *Scripta Materialia* 124: 164–168. DOI: 10.1016/j.scriptamat.2016.07.010

21. Elmer, J. W., Palmer, T. A., Zhang, W., Wood, B., and DebRoy, T. 2003. Kinetic modeling of phase transformations occurring in the HAZ of C-Mn steel welds based on direct observations. *Acta Materialia* 51(12): 3333–3349. DOI: 10.1016/S1359-6454(03)00049-1

22. Yurioka, N., Suzuki, H., Ohshita, S., and Saito, S. 1983. Determination of necessary preheating temperature in steel welding. *Welding Journal* 62(6): 147-s to 153-s.

23. Kasatkin, O. G., Vinokur, B. B., and Pilyushenko, V. L. 1984. Calculation models for determining the critical points of steel. *Metal Science and Heat Treatment* 26(1): 27–31. DOI: 10.1007/BF00712859

24. Lee, Y. K. 2002. Empirical formula of isothermal bainite start temperature of steels. *Journal of Materials Science Letters* 21(16): 1253–1255. DOI: 10.1023/A:1016555119230

25. Capdevila, C., Caballero, F. G., and García de Andrés, C. 2002. Determination of Ms temperature in steels: A Bayesian neural network model. *ISIJ International* 42(8): 894–902. DOI: 10.2355/isijinternational.42.894

26. Ronda, J., and Oliver, G. J. 2000. Consistent thermo-mechano-metallurgical model of welded steel with unified approach to derivation of phase evolution laws and transformation-induced plasticity. *Computer Methods in Applied Mechanics and Engineering* 189(2): 361–418. DOI: 10.1016/S0045-7825(99)00461-2

27. Xu, Z., and Zhao, L. C. 2004. *Theory of Metal Solid Phase Transformation*. Peking: Science Press. In press (In Chinese).

28. Mi, G., Zhan, X., Wei, Y., Ou, W., Gu, C., and Yu, F. 2015. A thermal-metallurgical model of laser beam welding simulation for carbon steels. *Modelling and Simulation in Materials Science and Engineering* 23: 035010. DOI: 10.1088/0965-0393/23/3/035010

29. Rees, G. I., and Bhadeshia, H. 1999. Bainite transformation kinetics, Part 1, Modified model. *Materials Science & Engineering A: Structural Materials: Properties, Microstructure and Processing* 8: 985–93.

30. Bhadeshia, H. K. D. H. 1982. Thermodynamic analysis of isothermal transformation diagrams. *Metal Science* 16(3): 159–165. DOI: 10.1179/030634582790427217

31. Morales-Rivas, L., Garcia-Mateo, C., Kuntz, M., Sourmail, T., and Caballero, F. G. 2016. Induced martensitic transformation during tensile test in nanostructured bainitic steels. *Materials Science and Engineering A* 662: 169–177. DOI: 10.1016/j.msea.2016.03.070

32. Doane, D. V., and Kirkaldy, J. S. 1978. *Hardenability Concepts with Applications to Steels*. New York, N.Y.: Metallurgical Society of AIME.

33. Kim, J. H., and Nakamichi, M. 2014. Effect of grain size on the hardness and reactivity of plasma-sintered beryllium. *Journal of Nuclear Materials* 453(1–3): 22–26. DOI: 10.1016/j.jnucmat.2014.06.019

34. Chokshi, A. H., Rosen, A., Karch, J., and Gleiter, H. 1989. On the validity of the Hall-Petch relationship in nano crystalline materials. *Scripta Metallurgica* 23(10): 1679–1684. DOI: 10.1016/0036-9748(89)90342-6

35. Voyiadjis, G. Z., and Yaghoobi, M. 2015. Large scale atomistic simulation of size effects during nanoindentation: Dislocation length and hardness. *Materials Science and Engineering A* 634: 20–31. DOI: 10.1016/j.msea.2015.03.024

36. Nix, W. D., and Gao, H. 1998. Indentation size effects in crystalline materials: A law for strain gradient plasticity. *Journal of the Mechanics and Physics of Solids* 46(3): 411–425. DOI: 10.1016/S0022-5096(97)00086-0

37. Pavlina, E. J., and Van Tyne, C. J. 2008. Correlation of yield strength and tensile strength with hardness for steels. *Journal of Materials Engineering and Performance* 17(6): 888–893. DOI: 10.1007/s11665-008-9225-5

38. Yu, M., Meng, F. Y., Liang, C., and An, J. 2013. Method for evaluating yield strength of laser weldments of maraging steels using hardness test. *Materials Science and Technology* 29(11): 1317–1323. DOI: 10.1179/1743284713Y.0000000275

39. Pavlina, E. J., and Van Tyne, C. J. 2014. Uniform elongation and the stress-strain flow curve of steels calculated from hardness using empirical correlations. *Journal of Materials Engineering and Performance* 23(6): 2247–2254. DOI: 10.1007/s11665-014-1037-1

40. Tiryakioğlu, M. 2015. On the relationship between Vickers hardness and yield stress in Al-Zn-Mg-Cu Alloys. *Materials Science and Engineering A* 633: 17–19. DOI: 10.1016/j.msea.2015.02.073

**LU WANG, YOUMIN RONG, YU HUANG** (*yuhuang7208@163.com*), **JIAJUN XU, JIANG HU,** and **GUOJUN ZHANG** are with the State Key Lab of Digital Manufacturing Equipment and Technology and the School of Mechanical Science and Engineering, Huazhong University of Science and Technology, Wuhan, China.